

Video Article

# Longitudinal Morphological and Physiological Monitoring of Three-dimensional Tumor Spheroids Using Optical Coherence Tomography

Yongyang Huang<sup>1</sup>, Jinyun Zou<sup>1</sup>, Mudabbir Badar<sup>1</sup>, Junchao Liu<sup>1</sup>, Wentao Shi<sup>5</sup>, Shunqiang Wang<sup>2</sup>, Qiongyu Guo<sup>3</sup>, Xiaofang Wang<sup>1</sup>, Sarah Kessel<sup>4</sup>, Leo Li-Ying Chan<sup>4</sup>, Peter Li<sup>4</sup>, Yaling Liu<sup>2,5</sup>, Jean Qiu<sup>4</sup>, Chao Zhou<sup>1,5,6</sup>

<sup>1</sup>Department of Electrical and Computer Engineering, Lehigh University

<sup>2</sup>Department of Mechanical Engineering, Lehigh University

<sup>3</sup>Department of Biomedical Engineering, Southern University of Science and Technology

<sup>4</sup>Department of Technology R&D, Nexcelom Bioscience LLC

<sup>5</sup>Department of Bioengineering, Lehigh University

<sup>6</sup>Center for Photonics and Nanoelectronics, Lehigh University

Correspondence to: Chao Zhou at [chz212@lehigh.edu](mailto:chz212@lehigh.edu)

URL: <https://www.jove.com/video/59020>

DOI: [doi:10.3791/59020](https://doi.org/10.3791/59020)

Keywords: Cancer Research, Issue 144, optical coherence tomography, OCT, cellular spheroids, cultured tumor cells, high-throughput screening assays, three-dimensional imaging, optical imaging, antitumor drug screening assays

Date Published: 2/9/2019

Citation: Huang, Y., Zou, J., Badar, M., Liu, J., Shi, W., Wang, S., Guo, Q., Wang, X., Kessel, S., Chan, L.L., Li, P., Liu, Y., Qiu, J., Zhou, C. Longitudinal Morphological and Physiological Monitoring of Three-dimensional Tumor Spheroids Using Optical Coherence Tomography. *J. Vis. Exp.* (144), e59020, doi:10.3791/59020 (2019).

## Abstract

Tumor spheroids have been developed as a three-dimensional (3D) cell culture model in cancer research and anti-cancer drug discovery. However, currently, high-throughput imaging modalities utilizing bright field or fluorescence detection, are unable to resolve the overall 3D structure of the tumor spheroid due to limited light penetration, diffusion of fluorescent dyes and depth-resolvability. Recently, our lab demonstrated the use of optical coherence tomography (OCT), a label-free and non-destructive 3D imaging modality, to perform longitudinal characterization of multicellular tumor spheroids in a 96-well plate. OCT was capable of obtaining 3D morphological and physiological information of tumor spheroids growing up to about 600  $\mu\text{m}$  in height. In this article, we demonstrate a high-throughput OCT (HT-OCT) imaging system that scans the whole multi-well plate and obtains 3D OCT data of tumor spheroids automatically. We describe the details of the HT-OCT system and construction guidelines in the protocol. From the 3D OCT data, one can visualize the overall structure of the spheroid with 3D rendered and orthogonal slices, characterize the longitudinal growth curve of the tumor spheroid based on the morphological information of size and volume, and monitor the growth of the dead-cell regions in the tumor spheroid based on optical intrinsic attenuation contrast. We show that HT-OCT can be used as a high-throughput imaging modality for drug screening as well as characterizing biofabricated samples.

## Video Link

The video component of this article can be found at <https://www.jove.com/video/59020/>

## Introduction

Cancer is the second leading cause of death in the world<sup>1</sup>. Developing drugs targeting cancer is of crucial importance for patients. However, it is estimated that more than 90% of new anti-cancer drugs fail in the development phase because of a lack of efficacy and unexpected toxicity in clinical trials<sup>2</sup>. Part of the reason can be attributed to the use of simple two-dimensional (2D) cell culture models for compound screening, which provide results with limited predictive values of compound efficacy and toxicity for the following stages of drug discovery<sup>2,3,4</sup>. Recently, three-dimensional (3D) tumor spheroid models have been developed to provide clinically relevant physiological and pharmacological data for anti-cancer drug discovery<sup>3,4,5,6,7,8,9,10,11,12,13,14,15,16,17,18,19,20,21,22,23,24,25</sup>. Since these spheroids can mimic tissue-specific properties of tumors *in vivo*, such as nutrient and oxygen gradient, hypoxic core as well as drug resistance<sup>19</sup>, the use of these models can potentially shorten drug discovery timelines, reduce costs of investment, and bring new medicines to patients more effectively. One critical approach to evaluating compound efficacy in 3D tumor spheroid development is to monitor the spheroid growth and recurrence under treatments<sup>9,26</sup>. To do this, quantitative characterizations of the tumor morphology, involving its diameter and volume, with high-resolution imaging modalities, are imperative.

Conventional imaging modalities, such as bright-field, phase contrast<sup>7,9,22,24</sup>, and fluorescence microscopy<sup>8,9,16,18,22</sup> can provide a measurement of the spheroid's diameter but cannot resolve the overall structure of the spheroid in 3D space. Many factors contribute to these limitations, including penetration of the probing light in the spheroid; diffusion of the fluorescent dyes into the spheroid; emitting fluorescent signals from excited fluorescent dyes inside or on the opposite surface of the spheroid due to strong absorption and scattering; and depth-resolvability of these imaging modalities. This often leads to an inaccurate volume measurement. Development of the necrotic core in spheroids mimics necrosis in *in vivo* tumors<sup>6,10,15,19,25</sup>. This pathological feature is unlikely reproduced in 2D cell cultures<sup>19,25,27,28</sup>. With a spheroid size larger than 500  $\mu\text{m}$  in diameter, a three-layer concentric structure, including an outer layer of proliferating cells, a middle layer of quiescent cells, and a necrotic core, can be observed in the spheroid<sup>6,10,15,19,25</sup>, due to lack of oxygen and nutrients. Live and dead cell fluorescence imaging is the

standard approach to label the boundary of the necrotic core. However, again, penetrations of both these fluorescent dyes and visible light hinder the potential to probe into the necrotic core to monitor its development in its actual shape.

An alternative 3D imaging modality, optical coherence tomography (OCT) is introduced to characterize the tumor spheroids. OCT is a biomedical imaging technique that is capable of acquiring label-free, non-destructive 3D data from up to 1-2 mm depths in biological tissues<sup>29,30,31,32,33,34</sup>. OCT employs low-coherence interferometry to detect back-scattered signals from different depths of the sample and provides reconstructed depth-resolved images at micron-level spatial resolutions in both lateral and vertical directions. OCT has been widely adopted in ophthalmology<sup>35,36,37</sup> and angiography<sup>38,39</sup>. Previous studies have used OCT to observe the morphology of *in vitro* tumor spheroids in basement membrane matrix (e.g., Matrigel) and evaluate their responses to photodynamic therapy<sup>40,41</sup>. Recently, our group established a high-throughput OCT imaging platform to systematically monitor and quantify the growth kinetics of 3D tumor spheroids in multi-well plates<sup>42</sup>. Precise volumetric quantification of 3D tumor spheroids using a voxel counting approach and label-free necrotic tissue detection in the spheroids based on intrinsic optical attenuation contrast were demonstrated. This paper describes the details of how the OCT imaging platform was constructed and employed to obtain high-resolution 3D images of tumor spheroids. The step-by-step quantitative analyses of the growth kinetics of 3D tumor spheroids, including accurate measurements of spheroid diameter and volumes, is described. Also, the method of the non-destructive detection of necrotic tissue regions using OCT, based on the intrinsic optical attenuation contrast is presented.

## Protocol

### 1. Preparation of Cells

- Obtain cell lines from a qualified supplier.  
NOTE: Verify that cells from the cell lines of interest can form spheroid in the culture media or with the help of a substrate (basement membrane matrix like Matrigel). Look into the literature<sup>9</sup> or perform one round of a pre-experiment for a check.
- Thaw the frozen cells following the specific procedure provided by the cell-line supplier. A general procedure can be found elsewhere<sup>43</sup>.
- Culture the cells for 1-2 passages in 25 cm<sup>2</sup> culture flasks. The cells are then ready to use for 3D cell culture.
- Monitor the health status of the cells every day and maintain them in an incubator under standard conditions (37 °C, 5% CO<sub>2</sub>, 95% humidity). Refresh the media as needed.  
NOTE: The culture medium consists of DMEM (4.5 g/L glucose), 1% antibiotic-antimycotic, 10% fetal bovine serum. Subculture cells before they reach confluence in the culture flask. Follow the cell culture guideline provided by the supplier. A general procedure can be found elsewhere<sup>44</sup>.
- Perform 3D cell culture in multi-well plates based on the following general protocol<sup>9</sup>.
  - Remove the culture media from the culture flask and wash it with sterilized phosphate buffered saline (PBS, heated to 37 °C).
  - Resuspend the cells by adding 1 mL of trypsin ethylenediaminetetraacetic acid (EDTA, 0.5%) into the flask for 3 min. Then, add culture media to dilute the trypsin.
  - Transfer the cell suspension into a 15 mL centrifuge tube and centrifuge for 5 min at 500 x g and room temperature.
  - Remove the supernatant and resuspend cells with 4 mL of pre-warmed culture medium. Pipette one drop of sample onto a hemocytometer for cell counting to determine cell concentration. Dilute the cells to appropriate concentration for seeding (e.g., 3,000 cells/mL).  
NOTE: Optimize the initial cell concentration of the spheroid for each cell-line and each type of multi-well plate (96-well, 384-well or 1536-well).
  - Seed cells into an ultra-low attachment (ULA) round-bottomed multi-well plate. Add 200 µL of cells suspension into each well at the concentration of 3,000 cells/mL so that each well has about 600 cells.
  - At RT, centrifuge the whole plate using a plate adapter for 7 min, right after seeding, at a speed of 350 x g or the lowest speed available.  
NOTE: The centrifuge helps gather cells to the center of the well to facilitate forming a single, uniform spheroid. The centrifuge step is performed only once at the beginning to form the tumor spheroids. It will not be repeated when the tumor spheroids start growing.
  - Maintain the multi-well plate at 37 °C and 5% CO<sub>2</sub> in a culture incubator and refresh the culture media every 3 days.  
NOTE: Growth time may vary for different 3D culture conditions. In our study, 3,000 cells/mL is used for both U-87 MG and HCT 116 cell lines in 96-well plates, so that the spheroid can grow to ~500 µm in 4–7 days for HCT 116 cells. Consider adding media supplements and growth factors for different spheroid models, based on the general 3D culture protocol.
  - Perform OCT imaging of tumor spheroids every 3–4 days for a longitudinal study of their growth.  
NOTE: Recommended time points for OCT imaging would be day 4, day 7, day 11, day 14, day 18 and day 21.

### 2. High-throughput OCT Imaging Platform

NOTE: See referenced work<sup>29,30,31,32,33,34</sup> for a thorough review of principles and applications of OCT. See **Figure 1** and Huang *et al.*<sup>42</sup> for details of the custom OCT imaging system used in this study.

- Choose an appropriate broadband light source for the OCT system for tumor spheroid imaging.  
NOTE: Here, a superluminescent diode (SLD, **Figure 1A,B**) with a central wavelength of ~1,320 nm and ~110 nm bandwidth was used as a broadband light source.
- Construct the reference arm and sample arm of the OCT system following the schematics (See **Figure 1A,B** for details). See the **Table of Materials** for a list of optical components to construct the OCT system. Ensure that the optical path length of the reference arm and sample arm are closely matched.
- Construct the spectrometer, including a collimator, a grating, an F-theta lens and a line-scan camera (See **Figure 1C** for setup<sup>34</sup>) for details of spectrometer design of OCT. Alternatively, select a commercial spectrometer that matches the center wavelength of the light source. Make

sure that the spectrometer is aligned correctly to cover the entire laser bandwidth, to achieve high photon collection efficiency and to provide slow wash-out of the interference pattern.

4. Characterize the performance of the OCT system, including the following metrics such as sample arm power, total imaging depth, depth-dependent sensitivity, axial resolution, depth of focus and lateral resolution. Place a weak reflector (e.g., a mirror with a neutral density filter) as a sample to measure the depth-dependent sensitivity, axial resolution, and depth of focus. Place a USAF resolution test chart target as the sample to check the lateral resolution.

NOTE: See references<sup>34,45</sup> for definitions of metrics of OCT performance and protocols to characterize these metrics<sup>45</sup>. See **Table 1** for a list of measured parameters for the custom OCT system used in our study.

5. Select a motorized translation stage to provide horizontal movement of the multi-well plate to image tumor spheroids in different wells (See **Figure 1B**). Use a stage with a travel range larger than 108 mm x 72 mm to ensure a full scanning of all the wells of the multi-well plate. Use a 2D or 3D motorized translation stage with software control to enable precise location of each well and automation of the OCT system for high-throughput imaging.
6. Use a plate adapter or design a plate holder (by 3D printing) to hold the multi-well plate in a fixed position.
7. Correct the tilting and rotation of the multi-well plate using a 2D tilting stage and a rotation stage mounted on the translational stage (See **Figure 1D**), before conducting any OCT imaging to minimize variation of the focus plane from different wells. Use D2, D11, B6, D6, G6 as the guiding wells when monitoring their relative positions in the OCT images (**Figure 1A**).
8. Adjust the rotation of the plate to ensure the edges of the plate are parallel with the direction of stage movement so that the wells remain at the same horizontal positions in the OCT images (**Figure 1E**). Adjust the tilting of the plate to be parallel to the optical table so that the wells remain at the same vertical locations for OCT imaging (**Figure 1F**).

NOTE: Adjustment of the tilting angle and focus help optimize the OCT image quality for all the wells. However, variations of the height of culture media in different wells may cause changes in optical paths which may lead to defocusing of the spheroid image. Auto-focus may be implemented to control the focal plane of OCT imaging to achieve optimized image quality. The adjustment step does not resolve poor OCT image quality of the tumor spheroid due to the following issues: the spheroid decentering due to initial seeding location; spheroid elevation when embedded in biofabricated extracellular matrices; poor plate quality with large variations of the height of well bottoms. Additional software control with auto-focus or self-alignment functions can be implemented to optimize the performance of the OCT imaging system.

9. Use a custom computer program to control the OCT image acquisition and the stage movement to collect data from each well sequentially.

### 3. OCT Scanning and Processing of Tumor Spheroids

1. On the day of the OCT imaging of tumor spheroids, take the multi-well plate from the incubator. Transfer the multi-well plate under the OCT imaging system. Place it on top of the plate adapter.

NOTE: OCT imaging of tumor spheroids may be performed with the polystyrene plate lid on or off. However, the water condensations on the lid due to evaporation from the wells may affect light transmission and distort the light path, yielding less optimal OCT images from the spheroids.

2. Adjust the height of the plate by moving along the z-direction of the translation stage. Maintain the focal plane position at ~100–200  $\mu\text{m}$  below the top surface of each spheroid, to minimize the effect of the non-uniform depth-wise focal profile.
3. Set a proper OCT scanning range (e.g., 1 mm x 1 mm) in the custom software to cover the whole tumor spheroid according to its development stages. Click **Save Parameters** to save the setting.
4. Use the custom software to acquire 3D OCT images of tumor spheroids one by one for all the wells of the plate containing spheroids. Click the **Preview** button to view the preview image and click the **Acquire** button to acquire the OCT image.

NOTE: Ensure that the OCT spheroid data are collected when the stage is not in motion. The spheroid is usually located at the center of the U-bottom well. However, the spheroid may be shifted in the culture media when the stage is accelerating or decelerating due to the inertia of the spheroid in the culture media.

5. Process 3D OCT datasets of tumor spheroids to generate OCT structural images with a custom C++ processing code. See **Figure 2A** for a flowchart of post-processing of OCT data.

NOTE: See **Figure 4A** for the generated 3D OCT structural images.

1. See Chapter 5 of Drexler and Fujimoto<sup>34</sup> and Jian *et al.*<sup>46</sup> for detail descriptions of post-processing steps of OCT data. Calibrate the pixel size in all three dimensions. Re-scale the OCT structural images on corrected scales.

NOTE: The distance in the axial direction (z-direction) of OCT images is a measure of the optical path difference between the reference arm and sample arm. Thus, the refractive index of the sample (n) needs to be taken into consideration when calibrating the pixel size in the axial direction for rescaling. In our study, we use  $n = 1.37$  as the refractive index of the tumor spheroid<sup>42</sup>.

6. Generate the collage of spheroid images using 2D OCT Images in three cross-sectional XY, XZ, and YZ planes across the centroid of the spheroid. See **Figure 3C–E** for the representative output of collages of spheroid images. Perform image registration for all the spheroids, using the MATLAB function `fftreg`<sup>47</sup>, to ensure that the centroids of all the spheroid are located approximately at the same location.
7. Obtain 3D rendering of the spheroid using a commercial or custom software.

NOTE: The following steps show how to obtain the 3D rendering of tumor spheroids using a commercial software.

1. Load the 3D OCT data into the software.
2. Click the **Surpass** panel. Then, click **Add New Volume**. Choose the **Blend** mode to use for 3D rendering.
3. Adjust the viewing angle by dragging the image using the mouse pointer.

### 4. Morphological Quantification of 3D Tumor Spheroids

NOTE: A custom written code in MATLAB processes this quantification. Click the **Run** button to initiate the process. See **Figure 2B** for the flowchart of the steps of morphological quantification of spheroids.

1. Quantify spheroid diameter, height, and diameter-based volume.
  1. Select 2D OCT Images in three cross-sectional XY, XZ, and YZ planes that cross the centroid of the spheroid.

2. Measure the diameter and height of the spheroid in XY and XZ planes, respectively.
3. Calculate diameter-based spheroid volume using:  $V = \frac{1}{6}\pi d^3$ , with a presumption of the spherical shape of tumor.
2. Quantify voxel-based spheroid volume.
  1. Apply a 3D averaging filter on the OCT structural data of spheroid to remove speckles.
  2. Segment tumor spheroids using the Canny edge detection<sup>48</sup> filter, frame by frame, with a proper threshold separating the tumor spheroid region from the well bottom.
  3. Group connective voxels for 3D data (see built-in function: bwconncomp).
  4. Calculate the mean distance between each connective voxel in the group and the spheroid centroid (manually chosen), for each group. Identify the spheroid region as the group with the minimum mean distance.
  5. Count the number of voxels within the spheroid region and then multiply by the actual volume of an individual voxel (volume/voxel), yielding the total volume of the spheroid.

## 5. Dead-Cell Region Detection of 3D Tumor Spheroids

NOTE: In a homogeneous medium, OCT back-scattered intensity detected as a function of depth ( $I(z)$ ) can be described by the Beer-Lambert Law<sup>49</sup>:  $I(z) = I_0 e^{-2\mu z}$ , where  $z$  represents the depth,  $\mu$  is the optical attenuation coefficient, and  $I_0$  is the incident intensity to the

sample. Hence the derived optical attenuation coefficient can be expressed as:  $\mu = -\frac{1}{2} \frac{d \log I(z)}{dz}$ . Since OCT images are often plotted on a logarithmic scale, the slope of the OCT intensity profile can be retrieved to derive the optical attenuation coefficient. See **Figure 2C** for a flowchart of the generation of the optical attenuation maps.

1. Perform segmentation to remove unwanted regions outside the spheroid. Perform 3D average filter to suppress the speckle noise that is inherent in OCT images.
2. Obtain pixel-wise optical attenuation coefficients by linear fitting the log-scale OCT intensity profile over a certain depth range (moving window), extract its slope, and multiply the slope by  $-1/2$ .  
NOTE: The attenuation coefficient at each voxel within the segmented spheroid region is calculated based on the slope of OCT intensity profile in a 10-voxel depth window ( $\sim 40 \mu\text{m}$  in depth), with the voxel located in the middle of the window.
3. Apply the methods above (steps 5.1 and 5.2) to each axial scan in a frame and each frame in a 3D dataset containing the segmented spheroid region until optical attenuation coefficients for all voxels of the segmented spheroid region are calculated.
4. Perform the binary thresholding to highlight the high-attenuation region.  
NOTE: See Huang *et al.*<sup>42</sup> for the determination of threshold of the high-attenuation region using histogram analysis.
5. Highlight the binarized optical attenuation map on the original image to label the dead-cell region (blending). Generate the 3D-rendered image of the blended attenuation map to visualize the 3D distribution of the dead-cell region.

## 6. Histology and Immunohistochemistry

NOTE: Histology and immunohistochemistry (IHC) stained images of tumor spheroids are obtained to correlate with the corresponding OCT results.

1. At selected time points, select 1-2 tumor spheroids from the multi-well plate for histology and IHC staining. Use a pipette with the 1 mL pipette tips to transfer the spheroid from the well to a 1.5 mL centrifuge tube.  
NOTE: Cut the 1 mL pipette tip before transfer to ensure that the opening of the tip is larger than the size of the tumor spheroid to avoid damaging the structure of the spheroid.
2. Collect each tumor spheroid in a single 1.5 mL microcentrifuge tube filled with 10% formaldehyde and fix for 48 h.
3. Perform the histology and IHC processes for each spheroid, using standard paraffin embedding techniques.  
NOTE: Stain 5  $\mu\text{m}$  thick sections of tumor spheroids for hematoxylin and eosin (H&E) and terminal deoxynucleotidyl transferase dUTP nick end labeling (TUNEL) apoptosis detection. A counterstaining of hematoxylin is applied to TUNEL. A digital slide scanner was used to scan the stained sample and obtain high-resolution histological and IHC images.

## Representative Results

### High Throughput Optical Coherence Tomography Imaging of Spheroids in a 96-well Plate

**Figure 3** exhibits the result of HT-OCT scanning of a 96-well plate with HCT 116 tumor spheroids on Day 3. The sequential scan of the whole plate starts from the bottom-right well (H12). **Figure 3B** shows the flow chart of the software implementation of the HT-OCT system. After one spheroid data were collected and processed, the plate would move to next well, wait for  $\sim 2$  s to allow the spheroid to rest, and collect the next spheroid data. Each OCT data consist of  $400 \times 400 \times 1024$  voxels, which corresponded to an actual volume of  $1.0 \times 0.84 \times 2.3 \text{ mm}^3$ . **Figure 3C** shows a collage of *en-face* OCT images of HCT 116 spheroids generated from the processed data. The result is comparable with images from other 2D high-throughput imaging system<sup>22</sup>. Given the 3D imaging capability of the OCT, we could also generate the collage of 2D cross-sectional spheroid images from 96 wells (**Figure 3D**) to monitor spheroid heights and visualize spheroid inhomogeneity in the vertical direction. A collage of 3D-rendered spheroid images is also feasible from any predefined angle (**Figure 3E**) to visualize the overall 3D shape and evaluate the roundness of the spheroid. Note that the overall OCT imaging and process time for the whole 96-well plate would be  $\sim 21$  min and  $\sim 25$  min when the line-scan camera is running at a speed of 92 kHz and 47 kHz, respectively. See **Video 1** for an example.

## Longitudinal Morphological and Physiological Monitoring of the Tumor Spheroid

After we obtained the OCT structural images of tumor spheroids from the plate for multiple time points, we could further analyze these data by quantifying the morphological and physiological information of the tumor spheroids. **Figure 4** shows the different approaches to characterize tumor spheroids and obtain longitudinal morphological and physiological information from them.

**Figure 4B** shows different ways to visualize the tumor spheroid. With the aid of either commercial or free software, we could load the 3D data into the software and create a "volume" of the tumor spheroid (3D rendering), which shows the overall structure of tumor spheroid in 3D space. With proper thresholding, we could generate a surface plot of tumor spheroid (**Figure 4B**), which could be used to segment the spheroid and measure the volume. We could also generate the orthogonal slides (ortho slides) from different cross-section planes in different orientations (**Figure 4B**, XZ, YZ, and XY) and measure the diameter and height of the tumor spheroid from these ortho slides.

Gathering the OCT data of the same spheroid from multiple time point, we could quantify the morphological information and generate the growth curve of the spheroid to show its longitudinal changes. **Figure 4C** shows representative data of an HCT 116 tumor spheroid being monitored for 21 days. From the segmented data and ortho slides, we measured the diameter, height and voxel-based volume of the spheroid for all the time point, which were listed in the table. We also calculated the diameter-based volume for a comparison. The growth curves in size and volume were plotted, respectively. From the growth curves, we could see that this HCT 116 tumor spheroid followed a linear growth pattern in volume before day 11. Before this time point, the spheroid kept growing and maintained a relatively uniform shape. However, after day 11, the spheroid became disrupted, flattened and fully collapsed on day 21. The growth curve of voxel-based volumes clearly shows the trend, with a gradually decreased volumes after day 11.

Based on the OCT data, we can also obtain the physiological information of the distribution of dead-cells within the tumor spheroids by analyzing the pixel-by-pixel optical attenuation from 2D cross-sectional images. Following the methods illustrated in **Figure 2** and Protocol 5, we could quantitatively determine the dead-cell regions and monitor the growth of these regions as a function of time. **Figure 4D** shows a representative result of longitudinal tracking of the increase of dead-cell areas in the tumor spheroid. The areas highlighted in red, which had high optical attenuation, show the labeled necrotic areas. From the 3D rendered optical attenuation map during the 14 day development, we could see the red sector expanding, indicating the increase of the necrotic regions. As the percentage of the necrotic areas increased, the tumor spheroid could not maintain its perfect shape. Therefore, they would tend to disrupt and collapse, which were seen in the longitudinal monitoring of tumor morphology in **Figure 4C**.

The proposed nondestructive dead tissue region detection technique was verified by comparing OCT optical attenuation map of HCT 116 tumor spheroid with corresponding images obtained by histology and IHC. **Figure 4D** presents such a comparison with a Day 14 HCT 116 spheroid. A good match between the OCT attenuation map and corresponding H&E and TUNEL slices were found, which was indicated by analyzing the features within the regions in H&E and TUNEL slices marked by dash lines derived from the contour of OCT high attenuation regions. In H&E slices, the dead tissue regions were indicated by less dense and aggregated structure located within the dashed line region. In TUNEL slices, a good match was observed between high attenuation region and TUNEL-labeled apoptotic cellular region.



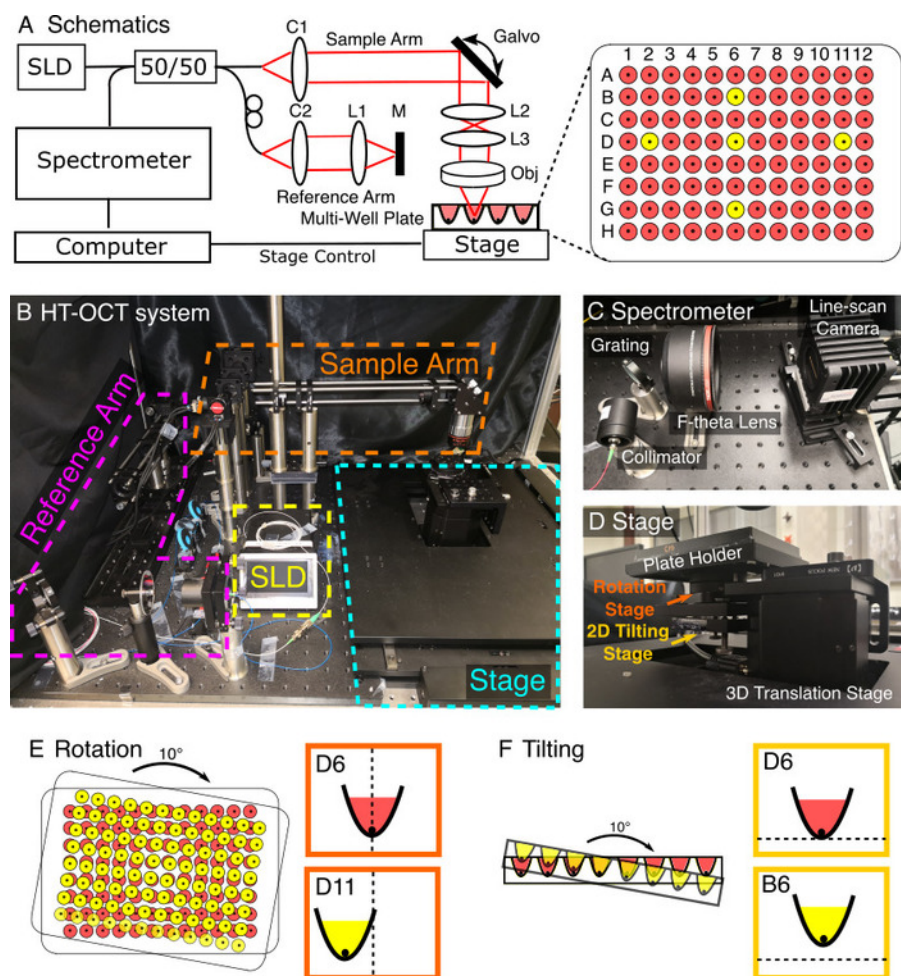
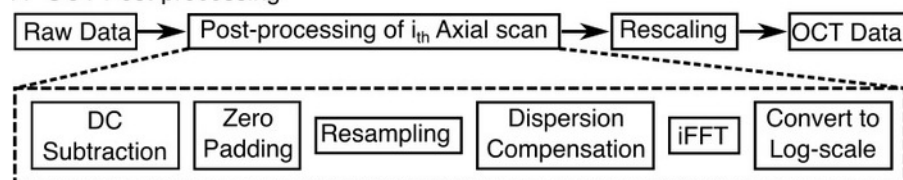
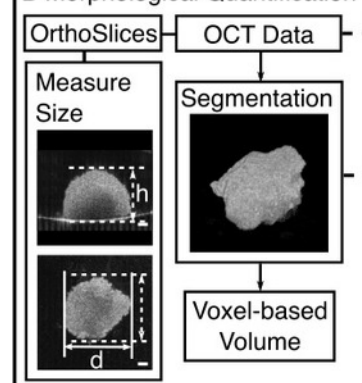


**Figure 1: Construction of a high-throughput optical coherence tomography (HT-OCT) system for tumor spheroid imaging.** (A) Schematics of the HT-OCT system. A diagram of the 96-well plate is plotted next to the OCT system. Five wells (D2, D11, B6, D6, G6) labeled in yellow are used for the fine adjustment of the stages in (D). (B) The actual configuration of HT-OCT system. See **Table of Materials** for optical components used for each part of the system. (C) Spectrometer design for the HT-OCT system. (D) Stage setup for the HT-OCT system. Proper alignment of the 6-axis stage and synchronization between the OCT acquisition and the stage movement are required for high-throughput imaging. (E) and (F) show the effects of rotation and tilting on final image of different wells. Rotation causes the OCT images of different wells to shift horizontally while tilting will lead to vertical shifting of different wells. [Please click here to view a larger version of this figure.](#)

# A OCT Post-processing



# B Morphological Quantification



# C Dead-cell region detection

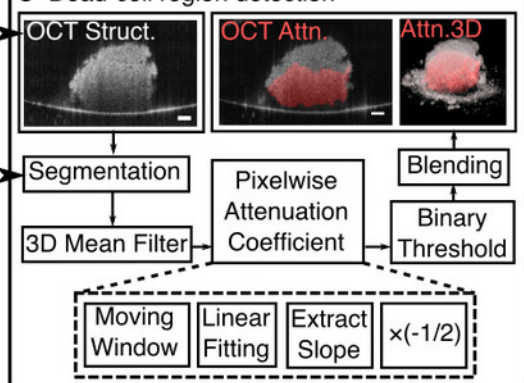


**Figure 2: Data Processing for OCT images of tumor spheroids.** (A) Flowchart of general post-processing steps for OCT data. (B) Flowchart of morphological quantification of the tumor spheroid. (C) Flowchart of dead cell region detection of the tumor spheroid. Scale bar: 100  $\mu\text{m}$  for all the subfigures. [Please click here to view a larger version of this figure.](#)

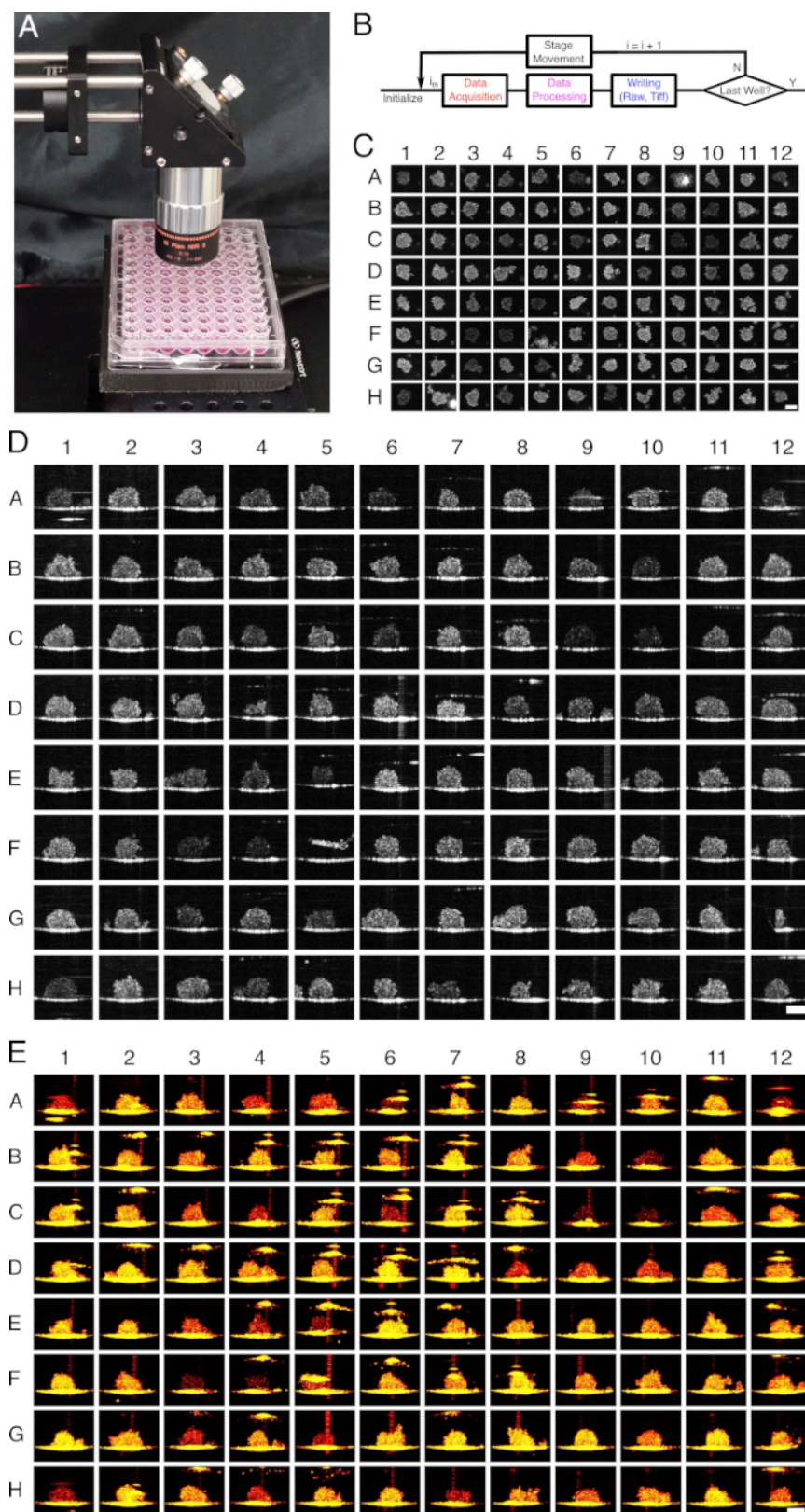


**Figure 3: High-throughput OCT scanning of a 96 well plate containing U-87 MG tumor spheroids.** (A) The actual setup with the 96-well plate under the objective. (B) Flow Chart of the software implementation of HT-OCT system. Collages of 96 *en face* (C), cross-sectional (D) and 3D rendered maximum intensity projection (MIP) (E) OCT images of Day 3 HCT 116 spheroids were generated from the processed data. Scale Bar: 200  $\mu$ m for all the subfigures. [Please click here to view a larger version of this figure.](#)



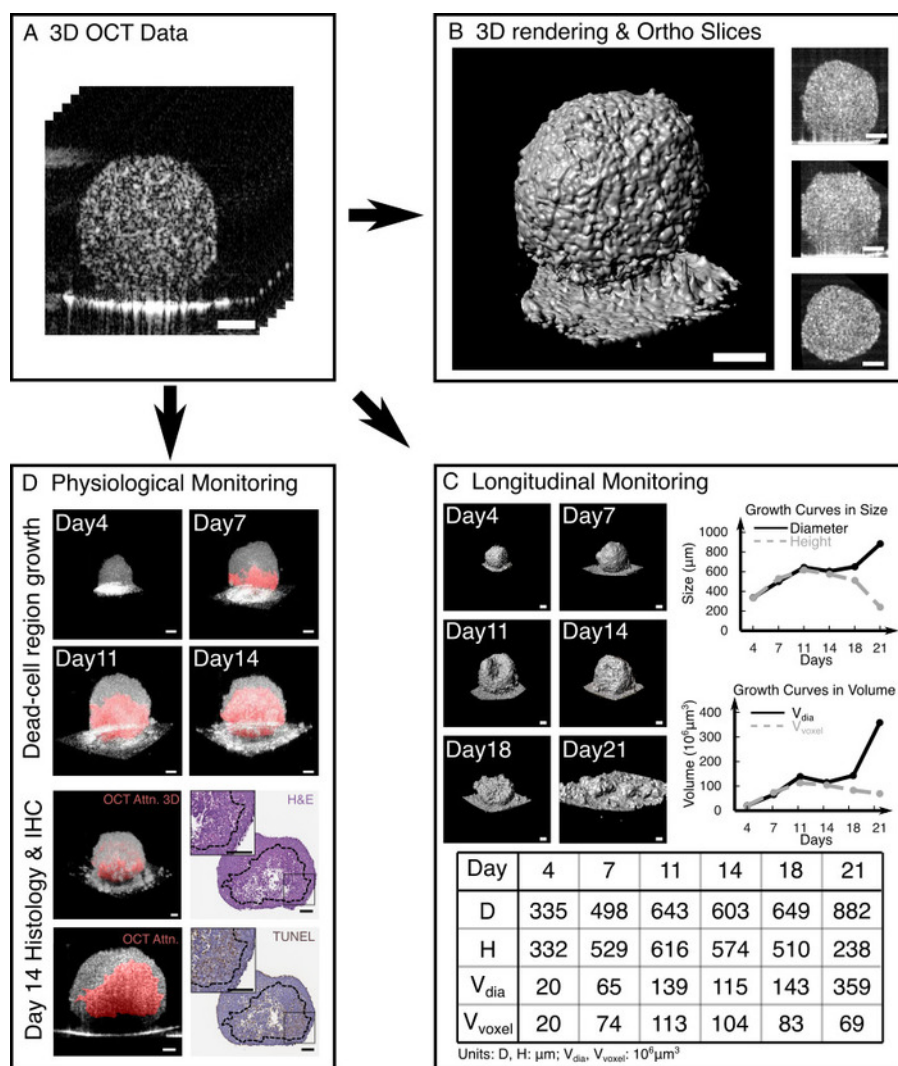
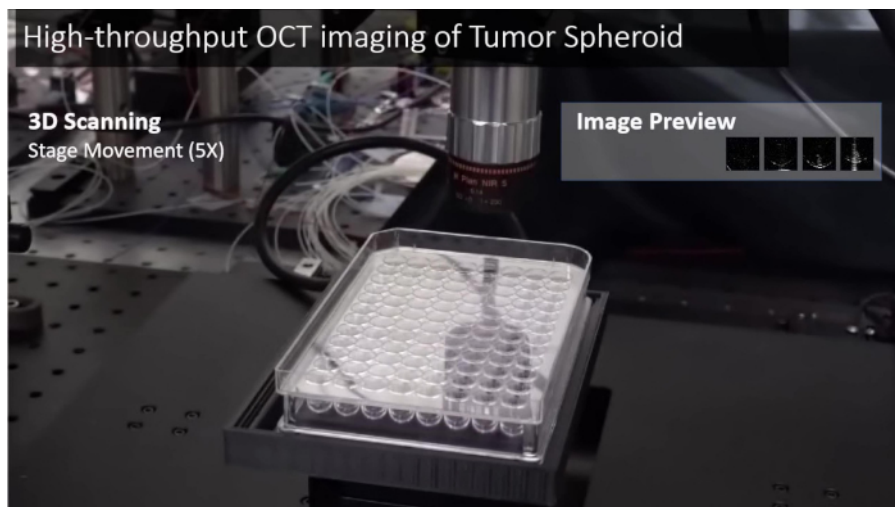


**Figure 4: Longitudinal Morphological and Physiological Quantification of Tumor Spheroids with 3D OCT data.** (A) Obtained 3D OCT structural images of a tumor spheroid after general OCT post-processing. From the OCT data, we can generate a 3D surface plot and XZ, YZ and XY orthogonal slices to visualize the structure of the tumor spheroid in any direction (B). We can perform longitudinal monitoring of a single tumor spheroid (C), characterizing its diameter, height and voxel-based volume (listed in the **Table of Materials**) and plotting the growth curves in size and volume during the 21-day development. In the example, as the spheroid developed, it became disrupted on day 11 and fully collapsed on day 21. We can further monitor the physiological status of a tumor spheroid longitudinally based on the optical intrinsic attenuation contrast (D). 3D rendered images of a tumor spheroid showed the appearance and growth of dead-cell regions from day 7 to day 14. The high-attenuation-labeled dead-cell areas in red were matched with histological and immunohistochemical (IHC) results. OCT attenuation map, H&E, and TUNEL result in **Figure 4D** are modified from Ref. 42. Scale bars: 100  $\mu\text{m}$  for all the subfigures. [Please click here to view a larger version of this figure.](#)



**Video 1: High-throughput OCT imaging of tumor spheroids.** A workflow of 3D OCT imaging, basic OCT processing and stage movement was presented in the video with a 5x speed. Previews of processed OCT structural images of spheroids were also presented. [Please click here to view this video.](#) (Right-click to download.)

## Discussion

Tumor activity is highly relevant to its morphological structure. Similar to monitoring characteristic growth curve for 2D cell cultures, tracking the growth curve for 3D tumor spheroids is also a conventional approach to characterize the long-term spheroid growth behavior for different cell lines. Notably, we can characterize the drug response by analyzing tumor degradation or tumor regrowth directly reflected in the growth curve. Therefore, quantitative assessment of 3D tumor spheroids, including the size and volume, to derive the growth curve, is of great importance for the characterization of tumor spheroids and the evaluation of compound effect. Currently, imaging platforms based on bright field, phase contrast or fluorescent imaging have been established for routine imaging and analysis of morphology or functions of the 3D tumor spheroids<sup>8,9,18,22</sup>. However, they are unable to resolve the entire, large tumor structure due to limited depth penetration as well as low-resolution depth-resolvability. In the representative results, we have demonstrated OCT to visualize the entire 3D structure of the tumor spheroid developing over time. 3D OCT imaging could provide the view of the spheroid in any orientation and any cross-section with high-resolvability, which was not available in conventional imaging modalities that lack the resolution along the depth. Furthermore, voxel-based volume quantification based on 3D OCT data yielded an accurate quantification of spheroid volumes without assuming their original shapes. Therefore, we have demonstrated that OCT is a robust imaging modality for 3D morphology characterization of tumor spheroids, which ensures accurate measurements of characteristic growth patterns for different cell lines and potentially can serve as an alternative for drug response evaluation.

Viability tests using fluorescent staining remain a popular approach for functional analyses of tumor spheroids, especially for drug screening<sup>18</sup>. However, the disruptive nature of fluorescent dyes indicates that these tests are only suitable for end-point studies. In our representative results (**Figure 4D**), we demonstrated an alternative method that can characterize cell viability within the entire spheroid. Our results have shown that OCT could distinguish the dead-cell region from the viable region in the spheroid based on intrinsic optical attenuation contrast. In addition, with 3D imaging capability and non-destructive nature of the OCT system, quantitative evaluation of the dead-cell distributions and *in situ* monitoring of the progression of dead-cell regions within the spheroid are feasible, which potentially provide more valuable information of the spheroid growth pattern. However, we should note that, in our representative results, we are not able to differentiate different types of cell death modes, such as apoptosis and necrosis, in the binary OCT attenuation map.

Since a drug compound library can be extensive (>10,000), a high-throughput and robust system to characterize tumor spheroids in multi-well plates during drug screening is imperative. The current high-throughput imaging system can achieve a screening of the whole 96-well plate in <5 min in 2D scan mode<sup>22</sup>. OCT can be adapted for high-throughput screening purpose, with the aid of a motorized stage. One can also obtain a commercially available OCT system (See **Table of Materials** for a list of commercial OCT systems) with a similar performance to our custom OCT system, and incorporate a motorized stage into the system. However, efforts must be taken to modify the commercial OCT system to integrate the motorized stage. Also, custom software implementation to realize the synchronization between the OCT acquisition trigger and stage movement trigger is required. For our prototype HT-OCT system, it took 2-18 seconds to acquire one 3D OCT data from a single tumor spheroid, depending on the choice of camera speed. Thus, the total acquisition time can be as short as ~3.2 min for a 96-well plate using HT-OCT system. However, the intermediate steps for the current HT-OCT system, including data processing, reading and writing data on hard drives, and stage movements, remained time consuming. Additional ~18 min would be needed on top of the ~3.2 min minimum data acquisition time. The total imaging time can be further reduced in several aspects: use state-of-the-art OCT systems equipped with a high-speed tunable laser source<sup>50,51</sup>; optimized the workflow by arranging critical steps (data acquisition, data processing, writing, stage movement) working in parallel; employ a parallel OCT imaging with a space-division multiplexing setup<sup>52</sup>. With system optimization, the high-throughput OCT system can be utilized in cancer drug discovery as well as characterization of other 3D bio-fabricated samples (e.g., 3D tissue organoids) for various biomedical applications.

## Disclosures

The authors disclose no competing interest.

## Acknowledgments

This work was supported by NSF grants IDBR (DBI-1455613), PFI:AIR-TT (IIP-1640707), NIH grants R21EY026380, R15EB019704 and R01EB025209, and Lehigh University startup fund.

## References

1. WHO. *Cancer*. <<http://www.who.int/cancer/en/>> (2018).
2. Kola, I., Landis, J. Can the pharmaceutical industry reduce attrition rates? *Nature Reviews Drug Discovery*. **3** (8), 711-716 (2004).
3. Breslin, S., O'Driscoll, L. Three-dimensional cell culture: the missing link in drug discovery. *Drug Discovery Today*. **18**, 240-249 (2013).
4. Hickman, J. A. *et al.* Three-dimensional models of cancer for pharmacology and cancer cell biology: Capturing tumor complexity in vitro/ex vivo. *Biotechnology Journal*. **9** (9), 1115-1128 (2014).
5. Sutherland, R. M. Cell and environment interactions in tumor microregions: the multicell spheroid model. *Science*. **240** (4849), 177-184 (1988).
6. Mueller-Klieser, W. Three-dimensional cell cultures: from molecular mechanisms to clinical applications. *American Journal of Physiology - Cell Physiology*. **273** C1109-C1123 (1997).
7. Friedrich, J., Seidel, C., Ebner, R., Kunz-Schughart, L. A. Spheroid-based drug screen: considerations and practical approach. *Nature Protocols*. **4** (3), 309-324 (2009).
8. Tung, Y.-C. *et al.* High-throughput 3D spheroid culture and drug testing using a 384 hanging drop array. *The Analyst*. **136** (3), 473-478 (2011).
9. Vinci, M. *et al.* Advances in establishment and analysis of three-dimensional tumor spheroid-based functional assays for target validation and drug evaluation. *BMC biology*. **10**, 29 (2012).
10. LaBarbera, D. V., Reid, B. G., Yoo, B. H. The multicellular tumor spheroid model for high-throughput cancer drug discovery. *Expert Opinion on Drug Discovery*. **7**, 819-830 (2012).
11. Pampaloni, F., Ansari, N., Stelzer, E. H. K. High-resolution deep imaging of live cellular spheroids with light-sheet-based fluorescence microscopy. *Cell and Tissue Research*. **352**, 161-177 (2013).
12. Lovitt, C. J., Shelper, T. B., Avery, V. M. Miniaturized three-dimensional cancer model for drug evaluation. *Assay and Drug Development Technologies*. **11** (7), 435-448 (2013).
13. Wenzel, C. *et al.* 3D high-content screening for the identification of compounds that target cells in dormant tumor spheroid regions. *Experimental Cell Research*. **323** (1), 131-143 (2014).
14. Astashkina, A., Grainger, D. W. Critical analysis of 3-D organoid in vitro cell culture models for high-throughput drug candidate toxicity assessments. *Innovative tissue models for drug discovery and development*. **69 - 70**, 1-18 (2014).
15. Edmondson, R., Broglie, J. J., Adcock, A. F., Yang, L. Three-dimensional cell culture systems and their applications in drug discovery and cell-based biosensors. *Assay and Drug Development Technologies*. **12** (4), 207-218 (2014).
16. Gong, X. *et al.* Generation of multicellular tumor spheroids with microwell-based agarose scaffolds for drug testing. *PLoS ONE*. **10** (6), e0130348 (2015).
17. Hoffmann, O. I. *et al.* Impact of the spheroid model complexity on drug response. *Journal of biotechnology*. **205**, 14-23 (2015).
18. Martinez, N. J., Titus, S. A., Wagner, A. K., Simeonov, A. High-throughput fluorescence imaging approaches for drug discovery using in vitro and in vivo three-dimensional models. *Expert Opinion on Drug Discovery*. **10**, 1347-1361 (2015).
19. Nath, S., Devi, G. R. Three-dimensional culture systems in cancer research: Focus on tumor spheroid model. *Pharmacology, Therapeutics*. **163**, 94-108 (2016).
20. Li, L., Zhou, Q., Voss, T. C., Quick, K. L., LaBarbera, D. V. High-throughput imaging: Focusing in on drug discovery in 3D. *Methods*. **96**, 97-102 (2016).
21. Ham, S. L., Joshi, R., Thakuri, P. S., Tavana, H. Liquid-based three-dimensional tumor models for cancer research and drug discovery. *Experimental Biology and Medicine*. **241** (9), 939-954 (2016).
22. Kessel, S. *et al.* High-Throughput 3D Tumor Spheroid Screening Method for Cancer Drug Discovery Using Celigo Image Cytometry. *Journal of Laboratory Automation*. 2211068216652846 (2016).
23. Stock, K. *et al.* Capturing tumor complexity in vitro: Comparative analysis of 2D and 3D tumor models for drug discovery. *Scientific Reports*. **6**, 28951 (2016).
24. Thakuri, P. S., Ham, S. L., Luker, G. D., Tavana, H. Multiparametric analysis of oncology drug screening with aqueous two-phase tumor spheroids. *Molecular Pharmaceutics*. **13** (11), 3724-3735 (2016).
25. Lin, R. Z., Chang, H. Y. Recent advances in three-dimensional multicellular spheroid culture for biomedical research. *Biotechnology Journal*. **3** (9-10), 1172-1184 (2008).
26. Piccinini, F., Tesei, A., Arienti, C., Bevilacqua, A. Cancer multicellular spheroids: Volume assessment from a single 2D projection. *Computer Methods and Programs in Biomedicine*. **118** (2), 95-106 (2015).
27. Zanoni, M. *et al.* 3D tumor spheroid models for in vitro therapeutic screening: a systematic approach to enhance the biological relevance of data obtained. *Scientific Reports*. **6**, 19103 (2016).
28. Debnath, J., Brugge, J. S. Modelling glandular epithelial cancers in three-dimensional cultures. *Nature Reviews Cancer*. **5** (9), 675-688 (2005).
29. Huang, D. *et al.* Optical coherence tomography. *Science*. **254** (5035), 1178-1181 (1991).
30. Drexler, W. *et al.* Optical coherence tomography today: speed, contrast, and multimodality. *Journal of Biomedical Optics*. **19** (7), 071412 (2014).
31. Fujimoto, J., Swanson, E. The development, commercialization, and impact of optical coherence tomography. *Investigative Ophthalmology, Visual Science*. **57** (9), OCT1-OCT13 (2016).
32. Vakoc, B. J., Fukumura, D., Jain, R. K., Bouma, B. E. Cancer imaging by optical coherence tomography: preclinical progress and clinical potential. *Nature Reviews Cancer*. **12** (5), 363-368 (2012).
33. Wojtkowski, M. High-speed optical coherence tomography: basics and applications. *Applied optics*. **49** (16), D30-D61 (2010).
34. Drexler, W., Fujimoto, J. G. *Optical coherence tomography: technology and applications*. Springer Science, Business Media (2008).

35. Geitzenauer, W., Hitzenberger, C. K., Schmidt-Erfurth, U. M. Retinal optical coherence tomography: past, present and future perspectives. *British Journal of Ophthalmology*. **95** (2), 171 (2011).
36. Sakata Lisandro, M., DeLeon-Ortega, J., Sakata, V., Girkin Christopher, A. Optical coherence tomography of the retina and optic nerve - a review. *Clinical, Experimental Ophthalmology*. **37** (1), 90-99 (2009).
37. van Velthoven, M. E. J., Faber, D. J., Verbraak, F. D., van Leeuwen, T. G., de Smet, M. D. Recent developments in optical coherence tomography for imaging the retina. *Progress in Retinal and Eye Research*. **26** (1), 57-77 (2007).
38. Kashani, A. H. *et al.* Optical coherence tomography angiography: A comprehensive review of current methods and clinical applications. *Progress in Retinal and Eye Research*. **60**, 66-100 (2017).
39. de Carlo, T. E., Romano, A., Waheed, N. K., Duker, J. S. A review of optical coherence tomography angiography (OCTA). *International Journal of Retina and Vitreous*. **1** (1), 5 (2015).
40. Sharma, M., Verma, Y., Rao, K. D., Nair, R., Gupta, P. K. Imaging growth dynamics of tumour spheroids using optical coherence tomography. *Biotechnology Letters*. **29** (2), 273-278 (2006).
41. Jung, Y., Nichols, A. J., Klein, O. J., Roussakis, E., Evans, C. L. Label-Free, Longitudinal Visualization of PDT Response In Vitro with Optical Coherence Tomography. *Israel Journal of Chemistry*. **52** (8-9), 728-744 (2012).
42. Huang, Y. *et al.* Optical coherence tomography detects necrotic regions and volumetrically quantifies multicellular tumor spheroids. *Cancer Research*. **77** (21), 6011-6020 (2017).
43. Spalteholz, W. *Über das Durchsichtigmachen von menschlichen und tierischen Präparaten: nebst Anhang. Über Knochenfärbung.* Verlag von S. Hirzel (1911).
44. Dodt, H.-U. *et al.* Ultramicroscopy: three-dimensional visualization of neuronal networks in the whole mouse brain. *Nature Methods*. **4** (4), 331 (2007).
45. Leitgeb, R., Hitzenberger, C., Fercher, A. F. Performance of fourier domain vs. time domain optical coherence tomography. *Optics express*. **11** (8), 889-894 (2003).
46. Jian, Y., Wong, K., Sarunic, M. V. in *Optical Coherence Tomography and Coherence Domain Optical Methods in Biomedicine XVII*. 85710Z International Society for Optics and Photonics (2013).
47. Guizar-Sicairos, M., Thurman, S. T., Fienup, J. R. Efficient subpixel image registration algorithms. *Optics Letters*. **33** (2), 156-158 (2008).
48. Canny, J. A computational approach to edge detection. *IEEE Transactions on Pattern Analysis and Machine Intelligence*. (6), 679-698 (1986).
49. Vermeer, K. A., Mo, J., Weda, J. J. A., Lemij, H. G., de Boer, J. F. Depth-resolved model-based reconstruction of attenuation coefficients in optical coherence tomography. *Biomedical Optics Express*. **5** (1), 322-337 (2014).
50. Klein, T. *et al.* Multi-MHz retinal OCT. *Biomedical Optics Express*. **4**, 1890-1908 (2013).
51. Klein, T., Huber, R. High-speed OCT light sources and systems [Invited]. *Biomedical Optics Express*. **8** (2), 828-859 (2017).
52. Zhou, C., Alex, A., Rasakanthan, J., Ma, Y. Space-division multiplexing optical coherence tomography. *Optics Express*. **21**, 19219-19227 (2013).